Mechanical, Bactericidal and Osteogenic Behaviours of Hydrothermally Synthesised TiO_2 Nanowire Arrays

Alka Jaggessar[a], Asha Mathew[b], Hongxia Wang[a], Tuquabo Tesfamichael[a], Cheng Yan[a] and Prasad KDV Yarlagadda[a]*

[a] Science and Engineering Faculty

Queensland University of Technology

2 George Street

Brisbane, QLD 4001

Australia.

[b] Institute of Health and Biomedical Innovation

Queensland University of Technology

60 Musk Avenue

Kelvin Grove, QLD 4059

Australia

* Correspondence: Prasad KDV Yarlagadda

y.prasad@qut.edu.au

Tel: +617 3138 5167

Fax: +617 3138 8381

Postal Address:

Science and Engineering Faculty

Queensland University of Technology

2 George Street

Brisbane, QLD 4001

Australia.

Alka Jaggessar: a.jaggessar@hdr.qut.edu.au

Asha Mathew: asha.mathew@qut.edu.au

Hongxia Wang: hx.wang@qut.edu.au

Tuquabo Tesfamichael: t.tesfamichael@qut.edu.au

Cheng Yan: c2.yan@qut.edu.au

Prasad KDV Yarlagadda: y.prasad@qut.edu.au

Abstract

The application of orthopaedic implants is associated with risks of bacterial infection and long-term antibiotic therapy. This problem has led to the study of implants with nano-textured surfaces as a method of inhibiting bacterial adhesion and reducing implant failure due to infection. In this research, various nano-textured surfaces of TiO_2 were synthesised using hydrothermal synthesis, by varying NaOH concentration, reaction time and reaction temperature. Their correlations to mechanical, morphological, bactericidal and osteogenic properties of the surfaces were investigated. It was found that high alkaline concentrations produced large nanowire mesh arrays, while short reaction time and low temperature produced comparatively smaller arrays. The highly dense morphology formed at higher NaOH concentrations has resulted in high elastic modulus and hardness values, compared to surfaces produced at lower NaOH concentrations. Viability tests of the TiO_2 nanowire array against gram-positive *Staphylococcus aureus* cells showed a bactericidal efficiency of 54% and 33% after 3 and 18 hours, respectively. This nano-textured surface produces an osteoblast cellular metabolic activity of 71% after 24 hours, compared to 67% when exposed to a flat Ti control surface. This preliminary work demonstrates an excellent outcome in producing bactericidal surfaces that promoted metabolic activity of human osteoblast cells for potential use in orthopaedic implants.

graphical abstract

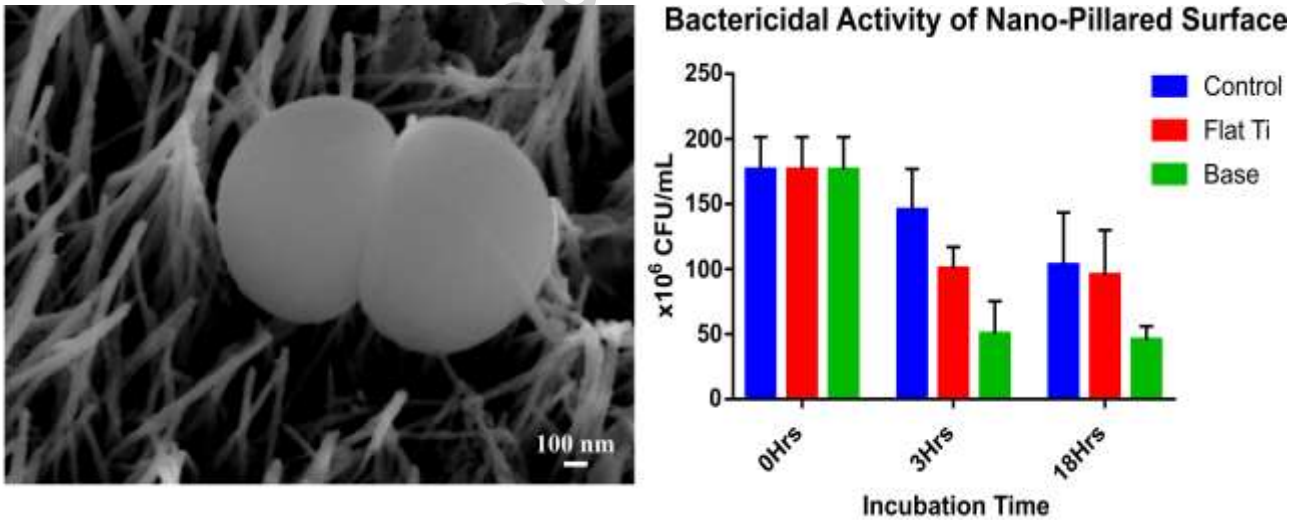

Keywords: Biomaterials; nano-textured surfaces; orthopaedic implants; bacterial adhesion; hydrothermal synthesis; mechanical properties[1].

1. Introduction

Implant failure due to infection accounts for approximately 23% of first revision surgeries (Association, 2016). This leads to increasing healthcare costs, hospitalization times, patient discomfort and long-term antibiotic use, contributing to bacterial resistance (Aboelzahab et al., 2012; Ahmed et al., 2012; Ferraris et al., 2016). Infection occurs through the formation of a polysaccharide matrix known as a biofilm, which protects bacteria from pharmacological treatment, antibiotic therapies and disinfectants (Arciola et al., 2012; Ferraris et al., 2016). The initial biofilm formation stage is dictated by cell-surface interaction, electrostatic and gravitation forces, hydrophobicity, and Van der Waal's forces. Surface roughness and topography also influence this initial biofilm formation stage (Hasan et al., 2015).

In the last few years, there has been a large interest in the surface structure of naturally occurring anti-biofouling and bactericidal surfaces to prevent bacterial adhesion to orthopaedic implants. Researchers have been inspired by the surface structures observed in some plant, animal and insect species (Cheng et al., 2006; Guo et al., 2007; Hasan et al., 2013; Jung et al., 2010; Kim, 2014; Ma et al., 2011; Ma et al., 2006; Pogodin et al., 2013). Mimicking of these naturally occurring micro and nano-textured surfaces on various substrate material have been attempted (Bhadra et al., 2015; Bixler et al., 2013; Dickson et al., 2015; Ivanova et al., 2013; Kesel et al., 2007; Sengstock et al., 2014). Titanium based textured surfaces have been found to reduce bacterial adhesion against some gram-negative and gram-positive bacteria strains (Bhadra et al., 2015; Diu et al., 2014; Lorenzetti et al., 2015; Oh et al., 2009; Sengstock et al., 2014; Tsimbouri et al., 2016; Zhu et al., 2014). Recent investigations also include fabrication of nanostructured surfaces using silicon (Bixler et al., 2013; Hsu et al., 2013; Ivanova et al., 2013; Zhang et al., 2006) and other polymer substrates (Dickson et al., 2015; Green et al., 2017; Liu et al., 2014; Nuzhdina et al., 2017; Pierret et al., 2010), with bactericidal properties ranging from 0 to 47% reduction in cell adhesion. Different fabrication techniques have been used to produce nano-textured structures, such as hydrothermal synthesis (Bhadra et al., 2015; Collazzo et al., 2011; Diu et al., 2014; Kolen'ko et al., 2006; Lim et al., 2010; Lorenzetti et al., 2015; Mali et al., 2011; Oh et al., 2009; Rao et al., 2012; Tsimbouri et al., 2016; Vu et al., 2014), lithography (soft, nano-imprint and colloidal) (Bixler et al., 2013; Dickson et al., 2015; Hsu et al., 2013; Liu et al., 2014; Pierret et al., 2010; Wang et al., 2017; Zhang et al., 2006) as well as various sputter and vapour deposition techniques (Ivanova et al., 2013; Sengstock et al., 2014; Zhang et al., 2017). While most lithography, focused ion beam milling and

[1] Abbreviations: *E. coli*, *Escherichia coli*; *P. aeruginosa*, *Pseudomonas aeruginosa*; *S. aureus*, *Staphylococcus aureus*; SEM, scanning electron microscopy; XRD, X-Ray Diffraction; OD, optical density; CFU, colony forming units; PBS, phosphate-buffered saline; Pen/Strep, Penicillin-Streptomycin; FBS, fetal bovine serum.

reactive ion etching methods have low associated costs, high resolution and low throughput, large-scale production using these methods still remains a challenge (Jaggessar et al., 2017).

Hydrothermal synthesis is a very commonly used method for fabricating nano-textured surfaces due to its reliability, environmentally friendly nature, simplicity, low cost compared to other methods, and flexibility for material morphology control (Bhadra et al., 2015; Zhu et al., 2014). High hydrothermal precursor concentration generally affects the morphology and increases the density of the fabricated structures (Wang et al., 2014). High precursor concentration affects the morphology and density of the fabricated surface. Increasing the precursor concentration has resulted in increased nanowire diameter and produces a highly dense and closely packed array (Wang et al., 2014). TiO_2 nano-textured surfaces have not been found to grow at temperatures below 100°C, where large particles of TiO_2 grow at temperatures above 180°C. Similarly, longer reaction time has produced larger particles (Liu et al., 2009; Ozel et al., 2015).

Black silicon (Ivanova et al., 2013; Linklater et al., 2017; Tian et al., 2017) and TiO_2 surfaces have been studied against gram-negative bacteria such as *Escherichia coli* (*E. coli*) and *Pseudomonas aeruginosa* (*P. aeruginosa*) (Diu et al., 2014; Lorenzetti et al., 2015; Sengstock et al., 2014). At the current stage of research, further work is required to make black silicon clinically relevant to implants (Linklater et al., 2017) due to the limitation in biocompatibility and mechanical nature of the material. TiO_2 is biocompatible and its nano-textured surface can be grown from Ti, which is a commonly used implant material. However, limited success has been achieved in creating TiO_2 as bactericidal surfaces against gram-positive bacteria, which is generally difficult to kill due to the increased number of peptidoglycan layers in the cell walls. In addition, the chemical and mechanical properties of the bactericidal material and their effect on osteoblast cellular response have not been well understood (Tsimbouri et al., 2016). Research has shown that increased surface roughness improves cell migration and attachment, enhancing osseointegration (Jemat et al., 2015). Currently, implants have various forms of coatings or ion implantation techniques to improve osseointegration and bone regeneration. These include silver nanoparticles, calcium phosphates and hydroxyapatite molecules to improve the acceptance of the implant into the body (Kulkarni et al., 2014; Leeuwenburgh et al., 2008; Shahali et al., 2017). However, these coatings may lose their effectiveness over time, leaking into the body causing toxicity repercussions (Briceno et al., 2017; Dickson et al., 2015).

This study aims to tailor the morphology and mechanical properties of TiO_2 nano-textured surfaces through modifying key parameters in the hydrothermal process (NaOH concentration, reaction time and reaction temperature). The bactericidal efficiency of the TiO_2 surfaces against gram-positive *Staphylococcus aureus* (*S.aureus*) cells and cellular metabolic activity of human osteoblast cells were evaluated. The outcomes are beneficial to the development of orthopaedic implants with robust mechanical performance and excellent bacterial resistance, while simultaneously promoting bone growth.

2. Experimental Design

2.1. Nanostructure Fabrication and Characterization

Hydrothermal synthesis was used to fabricate various nano-textured TiO_2 surfaces by varying NaOH concentration, hydrothermal reaction temperature and reaction time. Titanium plates (1 cm^2) were first polished to a surface roughness of 0.04 µm. Then the plates were sonicated in acetone and placed in a custom-made PTFE holder, in a 125 mL acid digestion vessel with 60 mL of NaOH. Different samples were produced by hydrothermal synthesis at a given temperature, reaction time and NaOH concentration (see Table 1). Samples were cooled to room temperature, annealed at 300°C for 1 hour, submerged in 0.6 M HCl for 30 minutes to form TiO_2 and lastly, heat treated for 2 hours at 600°C for calcination (Diu et al., 2014).

Scanning electron microscopy (SEM) was used to view surface topography of the samples. Images were taken at tilt angles of 40° using the Jeol JSM-7001F SEM at an accelerated voltage of 15 kV. Raman spectroscopy (Renishaw InVia Spectrometer with 532 nm laser, 10% laser power) and X-Ray Diffraction (XRD) were used to analyse crystalline phases. The relative weight percentage of anatase and rutile phases were obtained from XRD measurements. XRD was conducted using a Rigaku SmartLab diffractometer (Cu source, 40 kV, 40 mA), operating in parallel beam model with a Hypix 3000 detector (0D mode), with an incidence angle of 2° and scan axis 2Θ. Patterns were collected for 1 hour at a step size of 0.0152° in the range of 2θ = 5 – 75°. An instrument function was determined from LaB_6 (SRM 660A), which allowed for estimation of crystallite size, implemented in TOPAS using the double-Voigt approach (Haggerty et al., 2010; Rowles et al., 2010; Toraya et al., 1993). The crystallite size is taken as the mean volume weighted column length.

The mechanical properties of the surfaces were measured using nanoindentation (Hysitron TI 950), with a Berkovich indenter tip (three-sided pyramidal tip with an approximate radius of 100 nm and included angle of 142.3° (Xu et al., 2015)). The tip area function was calibrated using fused silica, with known elastic modulus and hardness. Each sample was indented at 10 points, using a trapezoid load function, with a loading rate of 20 µN/s and peak load of 200 µN. The loading rate was applied over 10 seconds, peak load held for 5 seconds, and then unloaded. Ti-6Al-4V (grade 5) (elastic modulus of 110 GPa and Poisson ration of 0.36) was used for further calibration and to confirm measurements. SEM images of the indentation craters were taken after using a peak force of 10 000 µN, in order to get a clear image of the indentation site.

2.2. Bacterial Viability Testing

Gram-positive *S. aureus* was chosen for this study as it is an important opportunistic human pathogen and is vital to orthopaedic implant applications (Ivanova et al., 2013). Bacterial viability testing was performed on the surfaces of the *Base* sample and polished titanium control sample using a standard plate count method. The *Base* surface was chosen for both bacterial viability and cellular metabolic activity tests in this preliminary work for its sharp nanopillar morphology. The other samples (*IncConc*, *RedTemp* and *RedTime*)

will be later tested as part of the future scope of this work. As titanium (and its alloys) is currently the material of choice for orthopaedic implants, polished flat titanium was used as the control surface for all bacteria and osteoblast testing. *S. aureus* (ATCC 25923) was suspended in 5 mL sterile nutrient broth and left to grow to an OD_{600} of 0.3. The suspension was then diluted using PBS, adjusting OD_{600} to 0.1. The re-suspended cells were diluted (1:10) and incubated at 37°C in triplicate with the sample. A well of the suspension without substrate material was used as a control to measure the natural death of the bacteria over time. 100 µL of each suspension was diluted, spread on nutrient agar plates and incubated for 24 hours at 37°C (sampled at 0, 3 and 18 hour time points). Resulting colonies were counted using ImageJ software, and colony forming units (CFU) per mL calculated. The bactericidal efficiency as a fraction of the number of cells at 0 hours was measured by the difference between the number of surviving cells and those remaining in the control at a given time point. The suspension was removed from the wall plates, and bacteria were fixed on samples using 3% glutaraldehyde ($C_5H_8O_2$), then washed in a 0.1 M cacodylate buffer, 1% OsT_4, ethanol series (from 50 – 100%) and lastly hexamethyldisiloxane ($C_6H_{19}NSi_2$). The samples were then gold coated to be imaged under SEM.

2.3. Cell Culture and AlamarBlue™ Assay

Human knee osteoblasts were obtained from a female donor after ethics approval (QUT HREC 1400001024). Bone with relatively non-osteoarthritic morphology (severe cartilage erosion and dense subchondral bone area) was collected, minced, washed with PBS, supplemented with Penicillin-Streptomycin (Pen/Strep) and vortexed. This process was repeated until the cloudy nature of the PBS disappeared after shaking. The bone chips were then transferred to a tissue culture flask, cultured at 37°C with culture medium (MEM-alpha supplemented with 10% FBS and Pen/Strep). Outgrowth of osteoblasts was observed after a few days, and cells were expanded and used at the seventh passage (P7).

Cellular metabolic activity was measured by the AlamarBlue™ assay, where dye reduction was considered proportional to the metabolic activity of the cells (Mathew et al., 2012). The activity was tested on both the *Base* and polished titanium surfaces. Cells seeded directly onto the tissue culture plate were set as the control. The cells were seeded onto each surface with a cell density of 10 000 cells/well in a 48 well tissue culture plate and incubated at 37°C with 500 µL cell culture medium (MEM-alpha supplemented with 10% FBS and Pen/Strep), for particular time points. AlamarBlue™ assay was conducted according to the manufacturer's instructions. Briefly, at each time point, culture medium was removed from each sample and washed three times with sterile PBS, and incubated for 2 hours with 10% AlamarBlue™ solution. After 2 hours incubation, absorbance at 550 and 595 nm was determined on a microplate reader (BIO RAD Benchmark Plus™) and the percentage reduction of the dye was calculated. Cells were then fixed in 3% glutaraldehyde, using the same process described for the *S. aureus* cells, and imaged under SEM. Statistical

analysis was performed by using a two-way ANOVA Tukey's multiple comparison test. Significant results are indicated in the figures, where * p<0.1, ** p<0.01, *** p<0.001 and **** p<0.0001.

3. Results

3.1. Surface Morphology

Figure 1 shows SEM topographical images of four samples obtained using different hydrothermal process parameters. While all topographies show random structure placement, spatial nanostructure arrangement and density, size varied greatly with changes in process parameters. The *Base* sample (Figure 1a) resulted in individual nanowires, randomly spaced and distinct from one another. From the four samples, the *Base* sample produced sharp nanowires with an average length of 298 ± 33 nm. The *IncConc* sample, where NaOH concentration was doubled (Table 1), shows a vastly different structure (Figure 1b) compared to *Base* samples (Figure 1a). An interconnected wire mesh is formed with large fibre lengths (approximately 690 – 1200 nm) compared to the individual nanopillars observed in other samples.

The *RedTemp* sample was obtained at a lower hydrothermal reaction temperature of 120°C. The topography of this sample (Figure 1c) is similar to that of the *Base* sample. However, the tips of the nanowires have been fused in some areas. The average height of these pillars is slightly larger than that of the *Base* sample (Table 2). However, the average diameter of the *RedTemp* sample appears smaller compared to the diameter of the *Base* sample (Table 2 summarises the morphology and average structure dimensions for each sample). The *RedTime* sample was made under a shorter reaction time of 1 hour producing very similar shape (Figure 1d) and diameter to the *RedTemp* sample. The structures of the *RedTemp* sample grow in a random manner with an average height of 251 ± 30 nm and diameter of 22 ± 3 nm. The orientation angle of the nanostructured arrays for all samples appear to be random.

3.2. Crystalline and Mechanical Properties

The crystal structure of the samples was examined by XRD and Raman Spectroscopy. The spectra obtained from both methods show a mixture of anatase and rutile TiO_2 as shown in Figure 2. Figure 2a displays the XRD patterns for the four sets of samples. The diffraction peaks that appear in the XRD patterns agree well with the diffraction peaks for rutile and anatase phases (Collazzo et al., 2011). However, the relative weight percentages and crystal sizes of both phases present in all samples vary across the different parameters tested.

Raman spectra (Figure 2b) confirms the presence of anatase and rutile phases in all samples. There is a major peak at 144 cm^{-1} corresponding to anatase (Mali et al., 2011), showing very strong intensity for both the *Base* and *IncConc* samples. The Raman intensity reduces for both the low reaction temperature (*RedTemp*) and low reaction time (*RedTime*) samples, suggesting lower degrees of crystallinity compared to

the *Base* and *IncConc* samples. In Figure 3a the relative weight percentage of rutile and anatase are insignificantly changed when the NaOH concentration is increased from 1 M to 2 M. This indicates that the NaOH concentration does not have a major influence on the relative weight percentages of the crystal phases in the hydrothermal process, and is consistent with previous reports (Liu et al., 2009). The results show that the factors affecting weight percentage of crystalline phases are reaction time and reaction temperature. At the higher reaction temperature (240°C) anatase is the dominating phase, whereas high relative weight percentages of rutile are obtained at a lower temperature and shorter reaction time. It can be said that as reaction time increases, some of the rutile is converted to anatase. It is possible that the formation of anatase is favoured under the reaction temperatures used in this work (Hanaor et al., 2011; Matthews, 1976).

Crystallite sizes also change with varying hydrothermal parameters, as seen in Figure 3b. The increase in NaOH concentration from 1 M (*Base*) to 2 M (*IncConc*) has produced larger crystallite sizes of 24.8 ± 1.2 nm (anatase) and 20.8 ± 1.0 nm (rutile). The increase in precursor concentration has caused an increase in growth and nucleation of the crystallites, increasing mean crystallite size (Yanqing et al., 2001). In contrast, increasing reaction temperature from 120°C (*RedTemp*) to 240°C (*Base*) results in smaller anatase and rutile crystallite sizes, indicating that crystal coalescence (sintering) is less effective at a lower temperature.

The elastic modulus and hardness of the samples were measured using nanoindentation. Load (*F*) vs. displacement (*h*) curves were constructed for each of the samples (Figure 4).

The hardness was calculated for each sample using Eq. (1) (Fischer-Cripps, 2011; Xu et al., 2015):

$$H = P_{max}/A_c \qquad \text{Eq. (1)}$$

Where H is the hardness of the material, P_{max} is the maximum applied load, and A_c is the contact area. Elastic modulus was found using Eq. 2 (Fischer-Cripps, 2011; Xu et al., 2015):

$$1/E_r = (1 - v_m^2)/E_m + (1 - v_i^2)/E_i \qquad \text{Eq. (2)}$$

Where E_r is the reduced modulus, E_m *and* v_m are the elastic modulus and Poisson ratio of the material, respectively, and E_i and v_i are the elastic modulus and Poisson ratio of the indenter, respectively. For a standard Berkovich diamond indenter probe the E_i is 1140 GPa and v_i is 0.07 (Fischer-Cripps, 2011). The v_m of the nano-arrays were chosen to be the same as bulk TiO_2 (0.28) (Xu et al., 2015). The average elastic moduli and hardness values of the surfaces are shown in Table 3.

The results of the nanoindentation test show that nanowires formed at low reaction times and temperatures (RedTemp and RedTime) have the highest overall Young's modulus and hardness values. However, as the indentation depth is between 38 to 53% of the average length of the pillars, it is likely that the properties of

the substrate have contributed towards the elastic modulus and hardness values measured for these samples. The densely packed morphology of the IncConc sample, as well as the large nanowire length and diameter obtained with 2 M NaOH, has resulted in a higher elastic modulus and hardness compared to the Base sample. The Base sample showed the lowest elastic modulus and hardness values (12.2 ± 2.3 GPa and 14.7 ± 1.8 MPa, respectively). Low hardness of the Base sample is reflected in Figure 4(b), where the unloading gradient (dP/dh) is steeper compared to other samples, indicating a lower comparative hardness. The RedTemp and RedTime samples have similar diameters (Table 2) and structure densities, producing similar mechanical properties. Existing literature has determined that the elastic modulus of TiO2 nano-arrays is between 4 to 43 GPa (Crawford et al., 2009; Xu et al., 2015). The hardness of the material is highly dependent on the fabrication process and material crystallinity (Xu et al., 2015). SEM images of the indentation craters (Figure 5) show the impression left by the three-faced Berkovich tip. While nanoindentation measurements were taken at a peak load of 200 µN, the slight impression left by the indenter tip, coupled with high surface roughness and randomness of the textured surface made these sites difficult to image. Indentations were repeated at a peak load of 10 000 µN and SEM images taken (Supplementary Data Figure 1). The images shows deformation, fractured and condensed structures, caused by the high load.

3.3. Bactericidal Efficiency

The bactericidal efficiency of the nanowire array (*Base* sample) was compared to a flat Ti-6Al-4V surface and a control sample against *S. aureus* cells. A standard viability plate-count method was applied during the investigation at 0, 3 and 18 hours incubation periods (Ivanova et al., 2013). Figure 6 shows the bactericidal activity of the nano-textured surface, flat Ti-6Al-4V surface and the control sample.

The results show that the CFU decreased over 18 hours with significant impact occurring as early as within the first 3 hours of incubation, similar to results obtained by Sengstock et al. (2014). On the basis of these results, the killing efficiency of the nano-pillared surface (*Base* sample) was found to be higher than the Ti-6Al-4V and control surfaces, supporting the hypothesis that the nano-textured surfaces inhibit bacterial adhesion. The *Base* sample was found to have an overall bactericidal efficiency of 71% after 3 hours, and around 74% after 18 hours. When taking into account the natural death of the cells, these efficiencies become 54% and 33% after 3 and 18 hours, respectively. Figure 7 shows SEM images of *S. aureus* cells that have attached to the flat Ti-6Al-4V and nano-textured TiO_2 surface (*Base* sample). From Figure 7c, the puncturing of the bacterium cell by the nano-pillars can be seen. SEM images of bacteria cells on the *Base* sample (Figure 7b and c) show that nanopillars were still intact after testing. Pillars were not deformed, bent or broken after contact with bacteria. This is to be expected, as the elastic modulus of the *Base* sample was found to be much higher than the Young's modulus that *S. aureus* cell walls acquire (0.0005 GPa) (Perry et al., 2009).

3.4. Human Osteoblast Metabolic Activity

AlamarBlue™ assay was performed to measure the cellular metabolic activity of human osteoblast cells on polished Ti-6Al-4V and nano-textured TiO_2 surfaces (*Base* sample), compared to a control. Figure 8 shows the AlamarBlue™ test results at 4 and 24 hours, with both flat and nano-textured surfaces causing a decrease in cell metabolism over the testing period, indicating certain levels of human cell death.

Both samples showed significantly reduced metabolic activity compared to the control cells. However, in both cases, the cellular metabolic activity did not fall below 67%. Although not significant, the nano-textured sample showed a slightly higher percentage of metabolic activity compared to the flat Ti-6Al-4V surface. Figure 9 shows SEM images of osteoblast cells attached to the tested surfaces at 4 and 24 hour incubation time.

4. Discussion

This study was designed to investigate the effect of alkaline concentration, reaction time and reaction temperature on the nano-textured morphology and mechanical properties of hydrothermally synthesized TiO_2 surfaces. It also aimed to investigate the efficiency of nano-textured TiO_2 surfaces against gram-positive bacteria, and to establish its effect on the cellular metabolic activity of human osteoblast cells. It is found that increasing NaOH concentration leads to the formation of a highly dense and closely packed nanowire mesh, due to the increased number of nucleation sites at higher NaOH concentrations. The nanowires in this dense array were grown at random angles to the substrate surface, causing wires to fuse with neighbouring nanowires (Liu et al., 2009), thereby creating a highly connected array (Figure 1b). As the hydrothermal reaction temperature increased from 120 to 240°C (*RedTime* and *Base* samples), shorter in length and larger diameter nanowires were grown (Figure 1d). As expected, the length of the nanowires increases with increasing reaction the time from 1 to 3 hours. From the observations, none of the samples possess uniform and vertically orientated nanowires.

The study showed crystallite size decreased with reaction time for anatase. It is possible that a longer reaction time has caused anatase crystals to divide and grow as new crystals, explaining the significant increase in relative weight percentages of anatase observed at longer reaction times. The formation of rutile and anatase highly depends on synthesis parameters. The transition from one phase to another is thermodynamically controlled and the kinetics of this transformation is dependent on the reaction temperature and time (Hanaor et al., 2011).

The mechanical properties were tested to see whether their mechanical stability of the nanostructures would be sufficient for implant applications. The mechanical performance of TiO_2 nanopillar arrays is not well understood, hence nanoindentation tests were completed to compare the mechanical properties of the structures fabricated under different hydrothermal conditions. The nano-patterned arrays need to maintain

adequate mechanical integrity for its application. As previously mentioned, increasing the NaOH precursor concentration from 1 to 2 M resulted in a significant change in the surface morphology. The lower NaOH concentration produced sharp, randomly spaced and oriented nanowires, the higher NaOH concentration tested produced a large, dense interconnected nanowire mesh. This in turn has produced a surface with higher mechanical properties. The TiO_2 nanowires produced in this work have the mechanical stiffness to withstand the presence of *S. aureus* bacteria and osteoblast cells, without mechanical damage (Figure 7b and c).

Although flat Ti-6Al-4V has antibacterial properties, the nano-textured TiO_2 surface structure causes cells to respond to the physical morphology and interaction forces of the structure (Ivanova et al., 2013). This leads to effective bactericidal activity and increases osteoblast cell growth. The deformation of peptidoglycan cell walls by the TiO_2 nano-textured surfaces result in cell death (Pogodin et al., 2013). The high killing efficiency of the nano-textured surface appears practical in inhibiting initial bacteria adhesion towards gram-positive bacteria and preventing further bacterial infection on the surface of implants. This is an important finding because killing of gram-positive bacteria cells have proven difficult. On the other hand, the nano-textured surface has produced a higher cellular metabolic activity than a flat surface at 3 and 18 hours. As the surface of medical implants currently used is flat Ti-6Al-4V, the results in this work indicate that osteoblast cell activity may increase with the presence of nano-textured surfaces. This enhancement of osteoblast cell growth by the nano-textured surface may be due to increased roughness and surface area, which improves cell migration and attachment as compared to a flat surface (Jemat et al., 2015). Osteoblast cell growth is highly favourable to reduce surgery recovery time, aid in improving the acceptance of the implant into the body and to improve bone remodelling, bone growth and implant fixation (Tsimbouri et al., 2016). The overall results demonstrate that the nano-textured surface improves osteoblast cell growth (compared to a flat surface) and accelerates gram-positive cell death.

5. Conclusion

This research explored the effect of NaOH concentration, reaction time and reaction temperature on the morphological and mechanical properties of TiO_2 nano-structures fabricated using hydrothermal synthesis. The results show that properties such as elastic modulus, hardness as well as morphology are strongly dependent on the NaOH concentration. From the parameters tested NaOH concentration appears to have the largest influence on surface morphology. Samples fabricated from 2 M NaOH showed a mesh-like nanowire structure with larger mechanical properties, whereas samples obtained from 1 M NaOH showed nano-textured surfaces with reduced strength. Bacterial viability tests demonstrated that the presence of nano-structured surfaces accelerate the natural death of gram-positive *S. aureus* cells. In addition, this nano-textured surface showed increased metabolic activity of human osteoblast cells compared to flat Ti-6Al-4V

surfaces. The overall results, with enhanced bactericidal activity to reduce infection in implants and increased osteoblast cell growth, are promising for the development of novel nanostructured materials in the biomedical field, which is the future scope of this work. This work is also being extended to include a wider range of data points for each hydrothermal reaction parameter using a factorial experimental design approach, as well as bacteria and osteoblast responses on the various surface topographies presented in this preliminary work. Modelling and sensitivity studies on the effect of hydrothermal process parameters on morphology and mechanical properties of topographies, is the ongoing work in this study.

Author Contributions

AJ performed hydrothermal synthesis, SEM and Raman spectroscopy, analysed XRD, nanoindentation, bacterial viability and osteoblast data, and wrote main manuscript. AJ and AM performed bacterial viability and osteoblast testing. HW assisted in hydrothermal experimental design. CY assisted in characterization methods. TT has assisted in the interpretation of characterization data. PKDVY has conceived the experiments, supervised and overseen the whole work, as well as approved the final version of the manuscript. All authors have reviewed and commented on the manuscript.

Acknowledgements

The authors would like to thank Dotmar Engineering Plastic Products for providing PFTE, Henry Spratt for performing the XRD measurements, Dilini Galpayage Dona for assisting nanoindentation tests, Donald McAuley for sample preparation, the Central Analytical Research Facility (QUT), Design and Manufacturing Centre (QUT), Institute for Future Environments (QUT) and Institute of Health and Biomedical Innovation (QUT).

Funding

This research was supported by the Queensland University of Technology, through the Research Training Program (RTP) Stipend.

Ethics Approval

Ethics approval for the use of female human knee osteoblast cells was obtained from the Queensland University of Technology (QUT HREC number 1400001024).

Competing Interests

The authors declare that there are no conflicting interests regarding this work.

References

Aboelzahab, A., Azad, A.-M., Dolan, S., Goel, V., 2012. Mitigation of Staphylococcus aureus -mediated surgical site infections with IR photoactivated TiO2 coatings on Ti implants, Adv. Healthc. Mater. 1 285-291. 10.1002/adhm.201100032.

Ahmed, M.H., Byrne, J.A., Keyes, T.E., Ahmed, W., Elhissi, A., Jackson, M.J., Ahmed, E., 2012. Characteristics and applications of titanium oxide as a biomaterial for medical implants, in: Davim, J. (Ed.), The Design and Manufacture of Medical Devices, Woodhead Publishing Ltd, Philadelphia, 2012, pp. 1-57.

Arciola, C.R., Campoccia, D., Speziale, P., Montanaro, L., Costerton, J.W., 2012. Biofilm formation in Staphylococcus implant infections. A review of molecular mechanisms and implications for biofilm-resistant materials, Biomaterials 33 5967-5982. 10.1016/j.biomaterials.2012.05.031.

Association, A.O., 2016. Hip, knee & shoulder arthroplasty: annnual report. <https://aoanjrr.sahmri.com/documents/10180/275066/Hip%2C%20Knee%20%26%20Shoulder%20Arthroplasty> (accessed 3 Mar 2017.).

Bhadra, C.M., Truong, V.K., Pham, V.T.H., Al Kobaisi, M., Seniutinas, G., Wang, J.Y., Juodkazis, S., Crawford, R.J., Ivanova, E.P., 2015. Antibacterial titanium nano-patterned arrays inspired by dragonfly wings, Sci. Rep. 5 16817. 10.1038/srep16817.

Bixler, G.D., Bhushan, B., 2013. Fluid drag reduction with shark-skin riblet inspired microstructured surfaces, Adv. Funct. Mater. 23 4507-4528. 10.1002/adfm.201203683.

Bixler, G.D., Bhushan, B., 2013. Rice- and butterfly-wing effect inspired self-cleaning and low drag micro/nanopatterned surfaces in water, oil, and air flow, Nanoscale 6 76-96. 10.1039/c3nr04755e.

Briceno, S., Hernandez, A.C., Sojo, J., Lascano, L., Gonzalez, G., 2017. Degradation of magnetite nanoparticles in biomimetic media, J Nanopart Res 19 1. 10.1007/s11051-017-3800-3.

Cheng, Y.T., Rodak, D.E., Wong, C.A., Hayden, C.A., 2006. Effects of micro- and nano-structures on the self-cleaning behaviour of lotus leaves, Nanotechnology 17 1359-1362. 10.1088/0957-4484/17/5/032.

Collazzo, G., Jahn, S., Carreño, N., Foletto, E., 2011. Temperature and reaction time effects on the structural properties of titanium dioxide nanopowders obtained via the hydrothermal method, Braz J Chem Eng 28 265-272.

Crawford, G.A., Chawla, N., Houston, J.E., 2009. Nanomechanics of biocompatible TiO2 nanotubes by Interfacial Force Microscopy (IFM), Journal of the Mechanical Behavior of Biomedical Materials 2 580-587. 10.1016/j.jmbbm.2008.10.004.

Dickson, M.N., Liang, E.I., Rodriguez, L.A., Vollereaux, N., Yee, A.F., 2015. Nanopatterned polymer surfaces with bactericidal properties, Biointerphases 10 021010. 10.1116/1.4922157.

Diu, T., Faruqui, N., Sjostrom, T., Lamarre, B., Jenkinson, H.F., Su, B., Ryadnov, M.G., 2014. Cicada-inspired cell-instructive nanopatterned arrays, Sci. Rep. 4 7122. 10.1038/srep07122.

Ferraris, S., Spriano, S., 2016. Antibacterial titanium surfaces for medical implants, Mater. Sci. Eng. C Mater. Biol. Appl. 61 965-978. 10.1016/j.msec.2015.12.062.

Fischer-Cripps, A.C., Nanoindentation, 3rd;3;Third; ed., Springer Verlag, New York, NY, 2011.

Green, D.W., Lee, K.K.H., Watson, J.A., Kim, H.Y., Yoon, K.S., Kim, E.J., Lee, J.M., Watson, G.S., Jung, H.S., 2017. High Quality Bioreplication of Intricate Nanostructures from a Fragile Gecko Skin Surface with Bactericidal Properties, Sci. Rep. 7 41023. 10.1038/srep41023.

Guo, Z., Liu, W., 2007. Biomimic from the superhydrophobic plant leaves in nature: Binary structure and unitary structure, Plant Sci. 172 1103-1112. 10.1016/j.plantsci.2007.03.005.

Haggerty, R.P., Sarin, P., Bérar, J.-F., Apostolov, Z.D., Kriven, W.M., 2010. Powder diffraction by fixed incident angle reflection using a curved position-sensitive detector, J Appl Crystallogr 43 560-569. 10.1107/S0021889810006400.

Hanaor, D.A.H., Sorrell, C.C., 2011. Review of the anatase to rutile phase transformation, J Mater Sci 46 855-874. 10.1007/s10853-010-5113-0.

Hasan, J., Chatterjee, K., 2015. Recent advances in engineering topography mediated antibacterial surfaces, Nanoscale 7 15568-15575. 10.1039/c5nr04156b.

Hasan, J., Webb, H.K., Truong, V.K., Pogodin, S., Baulin, V.A., Watson, G.S., Watson, J.A., Crawford, R.J., Ivanova, E.P., 2013. Selective bactericidal activity of nanopatterned superhydrophobic cicada Psaltoda claripennis wing surfaces, Appl. Microbiol. Biotechnol. 97 9257-9262. 10.1007/s00253-012-4628-5.
Hsu, L.C., Fang, J., Borca-Tasciuc, D.A., Worobo, R.W., Moraru, C.I., 2013. Effect of micro- and nanoscale topography on the adhesion of bacterial cells to solid surfaces, Appl. Environ. Microbiol. 79 2703-2712. 10.1128/AEM.03436-12.
Ivanova, E.P., Hasan, J., Webb, H.K., Gervinskas, G., Juodkazis, S., Truong, V.K., Wu, A.H.F., Lamb, R.N., Baulin, V.A., Watson, G.S., Watson, J.A., Mainwaring, D.E., Crawford, R.J., 2013. Bactericidal activity of black silicon, Nat. Commun. 4 2838. 10.1038/ncomms3838.
Jaggessar, A., Shahali, H., Mathew, A., Yarlagadda, P.K.D.V., 2017. Bio-mimicking nano and micro-structured surface fabrication for antibacterial properties in medical implants, Journal of Nanobiotechnology 15 64. 10.1186/s12951-017-0306-1.
Jemat, A., Ghazali, M.J., Razali, M., Otsuka, Y., 2015. Surface modifications and their effects on Titanium dental implants, BioMed Res Int 2015 791725. 10.1155/2015/791725.
Jung, Y.C., Bhushan, B., 2010. Biomimetic structures for fluid drag reduction in laminar and turbulent flows, J. Phys. Condens. Matter 22 035104. 10.1088/0953-8984/22/3/035104.
Kesel, A., Liedert, R., 2007. Learning from nature: Non-toxic biofouling control by shark skin effect, Comp. Biochem. Physiol., A: Mol. Integr. Physiol. 146 S130. 10.1016/j.cbpa.2007.01.246.
Kim, T.W., 2014. Assessment of hydro/oleophobicity for shark skin replica with riblets, J. Nanosci. Nanotechnol. 14 7562-7568.
Kolen'ko, Y.V., Kovnir, K.A., Gavrilov, A.I., Garshev, A.V., Frantti, J., Lebedev, O.I., Churagulov, B.R., Van Tendeloo, G., Yoshimura, M., 2006. Hydrothermal synthesis and characterization of nanorods of various titanates and titanium dioxide, J Phys Chem B 110 4030-4038. 10.1021/jp055687u.
Kulkarni, M., Mazare, A., Schmuki, P., Iglic, A., Seifalian, A., 2014. Biomaterial surface modification of titanium and titanium alloys for medical applications, Nanomedicine 111 111.
Leeuwenburgh, S.C.G., Wolke, J.G.C., Jansen, J.A., de Jonge, L.T., 2008. Organic-inorganic surface modifications for titanium implant surfaces, Pharm. Res. 25 2357-2369. 10.1007/s11095-008-9617-0.
Lim, Y.W.L., Tang, Y., Cheng, Y.H., Chen, Z., 2010. Morphology, crystal structure and adsorption performance of hydrothermally synthesized titania and titanate nanostructures, Nanoscale 2 2751-2757. 10.1039/c0nr00440e.
Linklater, D.P., Nguyen, H.K.D., Bhadra, C.M., Juodkazis, S., Ivanova, E.P., 2017. Influence of nanoscale topology on bactericidal efficiency of black silicon surfaces, Nanotechnology 28 9. 10.1088/1361-6528/aa700e.
Liu, B., Aydil, E.S., 2009. Growth of Oriented Single-Crystalline Rutile TiO2 Nanorods on Transparent Conducting Substrates for Dye-Sensitized Solar Cells, J. Am. Chem. Soc. 131 3985-3990. 10.1021/ja8078972.
Liu, W., Liu, X., Fangteng, J., Wang, S., Fang, L., Shen, H., Xiang, S., Sun, H., Yang, B., 2014. Bioinspired polyethylene terephthalate nanocone arrays with underwater superoleophobicity and anti-bioadhesion properties, Nanoscale 6 13845-13853. 10.1039/c4nr04471a.
Lorenzetti, M., Dogsa, I., Stosicki, T., Stopar, D., Kalin, M., Kobe, S., Novak, S., 2015. The influence of surface modification on bacterial adhesion to Titanium-based substrates, ACS Appl. Mater. Interfaces 7 1644-1651. 10.1021/am507148n.
Ma, J., Sun, Y., Gleichauf, K., Lou, J., Li, Q., 2011. Nanostructure on taro leaves resists fouling by colloids and bacteria under submerged conditions, Langmuir 27 10035-10040. 10.1021/la2010024.
Ma, M., Hill, R.M., 2006. Superhydrophobic surfaces, Curr. Opin. Colloid Interface Sci. 11 193-202. 10.1016/j.cocis.2006.06.002.
Mali, S.S., Shinde, P.S., Betty, C.A., Bhosale, P.N., Lee, W.J., Patil, P.S., 2011. Nanocoral architecture of TiO2 by hydrothermal process: Synthesis and characterization, Appl. Surf. Sci. 257 9737-9746. 10.1016/j.apsusc.2011.05.119.
Mathew, A., Cao, H., Collin, E., Wang, W., Pandit, A., 2012. Hyperbranched PEGmethacrylate linear pDMAEMA block copolymer as an efficient non-viral gene delivery vector, Int J Pharm 434 99-105. http://dx.doi.org/10.1016/j.ijpharm.2012.05.010.

Matthews, A., 1976. The crystallization of anatase and rutile from amorphous titanium dioxide under hydrothermal conditions, American Mineralogist 61 419-424.
Nuzhdina, A.V., Morozov, A.S., Kopitsyna, M.N., Strukova, E.N., Shlykova, D.S., Sessonov, I.V., Lobakova, E.S., 2017. Simple and versatile method for creation of non-leaching antimicrobial surfaces based on cross-linked alkylated polyethyleneimine derivatives, Mater. Sci. Eng. C Mater. Biol. Appl. 70 788-795. 10.1016/j.msec.2016.09.033.
Oh, J.-K., Lee, J.-K., Kim, S.J., Park, K.-W., 2009. Synthesis of phase- and shape-controlled TiO2 nanoparticles via hydrothermal process, J Ind Eng Chem 15 270-274. 10.1016/j.jiec.2008.10.001.
Ozel, F., Kockar, H., Karaagac, O., 2015. Growth of iron oxide nanoparticles by hydrothermal process: Effect of reaction parameters on the nanoparticle size, J Supercond Nov Magn 28 823-829. 10.1007/s10948-014-2707-9.
Perry, C.C., Weatherly, M., Beale, T., Randriamahefa, A., 2009. Atomic force microscopy study of the antimicrobial activity of aqueous garlic versus ampicillin against Escherichia coli and Staphylococcus aureus, J. Sci. Food Agric. 89 958-964. 10.1002/jsfa.3538.
Pierret, A., Hocevar, M., Diedenhofen, S.L., Algra, R.E., Vlieg, E., Timmering, E.C., Verschuuren, M.A., Immink, G.W.G., Verheijen, M.A., Bakkers, E.P.A.M., 2010. Generic nano-imprint process for fabrication of nanowire arrays, Nanotechnology 21 065305. 10.1088/0957-4484/21/6/065305.
Pogodin, S., Hasan, J., Baulin, V.A., Webb, H.K., Truong, V.K., Phong Nguyen, T.H., Boshkovikj, V., Fluke, C.J., Watson, G.S., Watson, J.A., Crawford, R.J., Ivanova, E.P., 2013. Biophysical model of bacterial cell interactions with nanopatterned cicada wing surfaces, Biophys. J. 104 835-840. 10.1016/j.bpj.2012.12.046.
Rao, X., Chu, C.L., Chung, C.Y., Chu, P.K., 2012. Hydrothermal Growth Mechanism of Controllable Hydrophilic Titanate Nanostructures on Medical NiTi Shape Memory Alloy, J Mater Eng Perform 21 2600-2606. 10.1007/s11665-012-0267-3.
Rowles, M.R., Madsen, I.C., 2010. Whole-pattern profile fitting of powder diffraction data collected in parallel-beam flat-plate asymmetric reflection geometry, J Appl Crystallogr 43 632-634. 10.1107/S0021889810007673.
Sengstock, C., Lopian, M., Motemani, Y., Borgmann, A., Khare, C., Buenconsejo, P.J.S., Schildhauer, T.A., Ludwig, A., Koller, M., 2014. Structure-related antibacterial activity of a titanium nanostructured surface fabricated by glancing angle sputter deposition, Nanotechnology 25 195101. 10.1088/0957-4484/25/19/195101.
Shahali, H., Jaggessar, A., Yarlagadda, P.K.D.V., 2017. Recent advances in manufacturing and surface modification of Titanium orthopaedic applications, Procedia Eng. 174 1067-1076. http://doi.org/10.1016/j.proeng.2017.01.259.
Tian, P., Guo, Z., 2017. Bioinspired silica-based superhydrophobic materials, Appl. Surf. Sci. 426 1-18. 10.1016/j.apsusc.2017.07.134.
Toraya, H., Huang, T.C., Wu, Y., 1993. Intensity enhancement in asymmetric diffraction with parallel-beam synchrotron radiation, J Appl Crystallogr 26 774-777. 10.1107/S0021889893004881.
Tsimbouri, P.M., Fisher, L., Holloway, N., Sjostrom, T., Nobbs, A.H., Meek, R.M.D., Su, B., Dalby, M.J., 2016. Osteogenic and bactericidal surfaces from hydrothermal titania nanowires on titanium substrates, Sci. Rep. 6 36857. 10.1038/srep36857.
Vu, T.H.T., Au, H.T., Tran, L.T., Nguyen, T.M.T., Tran, T.T.T., Pham, M.T., Do, M.H., Nguyen, D.L., 2014. Synthesis of titanium dioxide nanotubes via one-step dynamic hydrothermal process, J Mater Sci 49 5617-5625. 10.1007/s10853-014-8274-4.
Wang, M.D., Xing, C.C., Cao, K., Meng, L., Liu, J.B., 2014. Alignment-controlled hydrothermal growth of well-aligned ZnO nanorod arrays, J Phys Chem Solids 75 808-817. 10.1016/j.jpcs.2014.02.011.
Wang, W., Yang, G., Cui, H., Meng, J., Wang, S., Jiang, L., 2017. Bioinspired pollen-like hierarchical surface for efficient recognition of target cancer cells, Adv. Healthc. Mater. 6 1700003. 10.1002/adhm.201700003.
Xu, Y.N., Liu, M.N., Wang, M.C., Oloyede, A., Bell, J.M., Yan, C., 2015. Nanoindentation study of the mechanical behavior of TiO2 nanotube arrays, J Appl Phys 118. 10.1063/1.4932213.
Yanqing, Z., Erwei, S., Zhizhan, C., Wenjun, L., Xingfang, H., 2001. Influence of solution concentration on the hydrothermal preparation of titania crystallites, J Mater Chem 11 1547-1551. 10.1039/b009203g.

Zhang, G., Zhang, J., Xie, G., Liu, Z., Shao, H., 2006. Cicada wings: A stamp from nature for nanoimprint lithography, Small 2 1440-1443. 10.1002/smll.200600255.
Zhang, Y., Ma, H., Yi, M., Shen, Z., Yu, X., Zhang, X., 2017. Magnetron-sputtering fabrication of noble metal nanodots coated TiO2 nanoparticles with enhanced photocatalytic performance, Mater. Des. 125 94-99. http://dx.doi.org/10.1016/j.matdes.2017.03.084.
Zhu, K.X., Hu, G.X., 2014. Supercritical hydrothermal synthesis of titanium dioxide nanostructures with controlled phase and morphology, J Supercrit Fluids 94 165-173. 10.1016/j.supflu.2014.07.011.

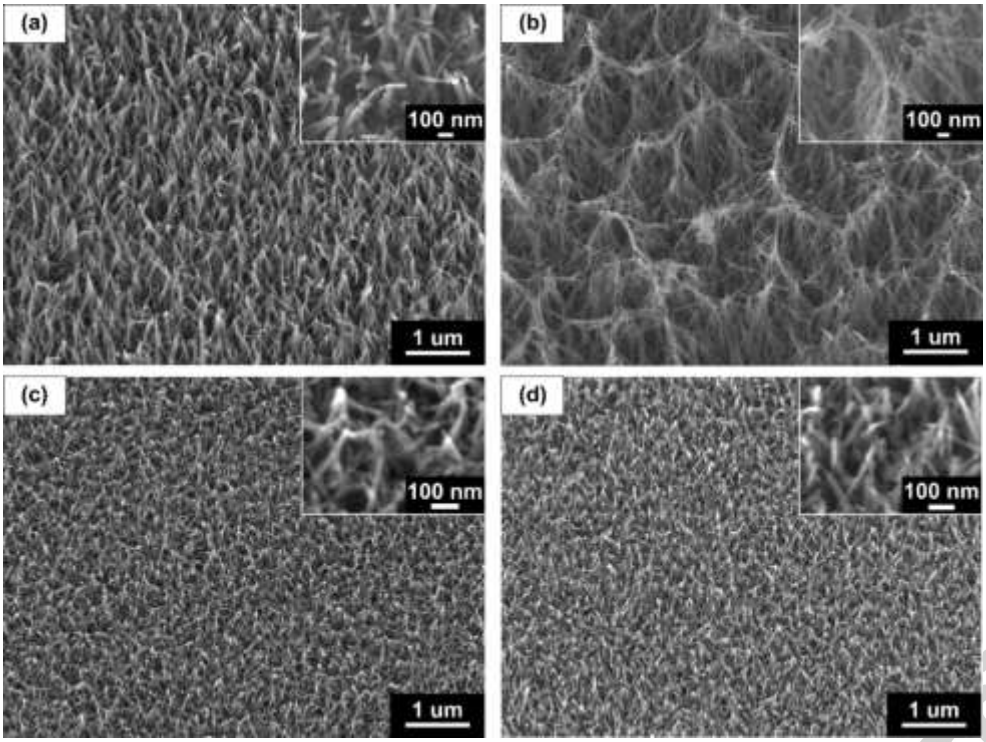

Figure 1: SEM images of TiO2 surfaces fabricated via hydrothermal synthesis using parameters shown in Table 1: (a) Base surface (b) IncConc surface, (c) RedTemp surface and (d) RedTime surface.

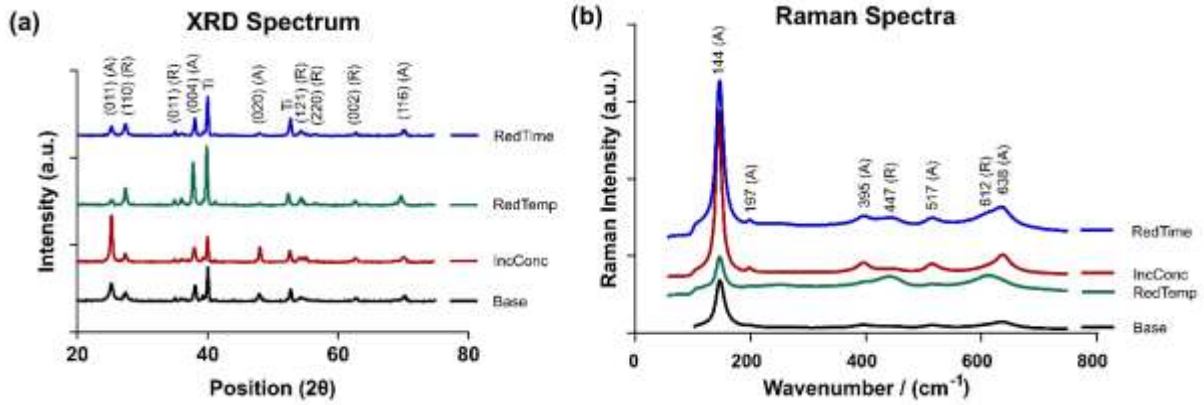

Figure 2: (a) XRD spectra and (b) Raman spectra of the hydrothermally synthesized TiO2 nanowire array samples.

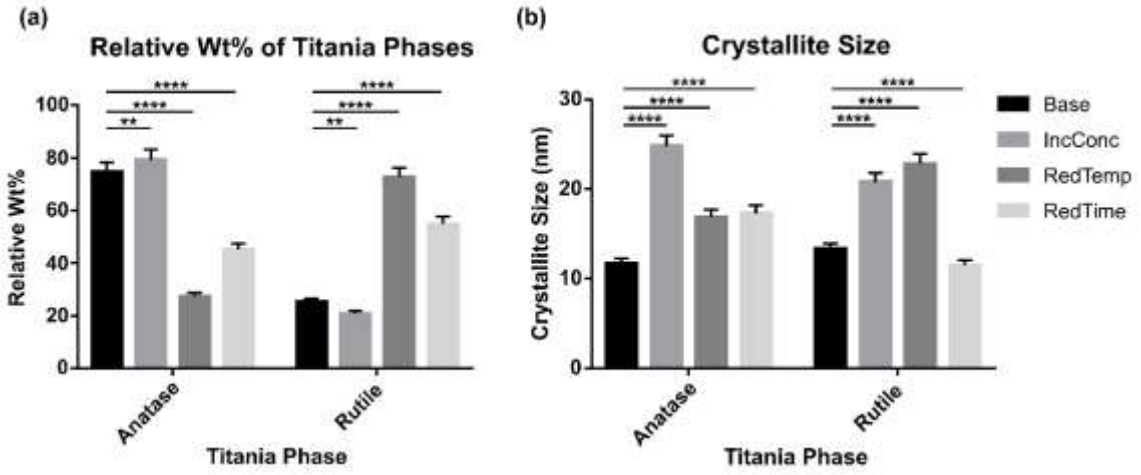

*Figure 3: (a) Crystallite size and (b) relative weight percentage of TiO2 phases for the samples fabricated using hydrothermal synthesis. Comparison by 2-way ANOVA **P<0.01 and ****P<0.0001.*

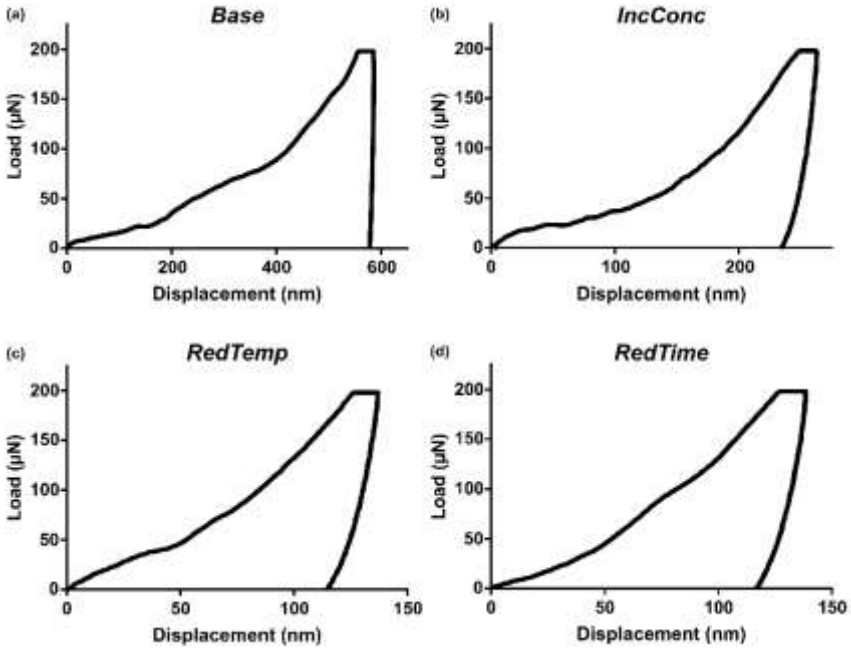

Figure 4: Load-displacement curves for (a) Base, (b) IncConc, (c) RedTemp, and (d) RedTime samples.

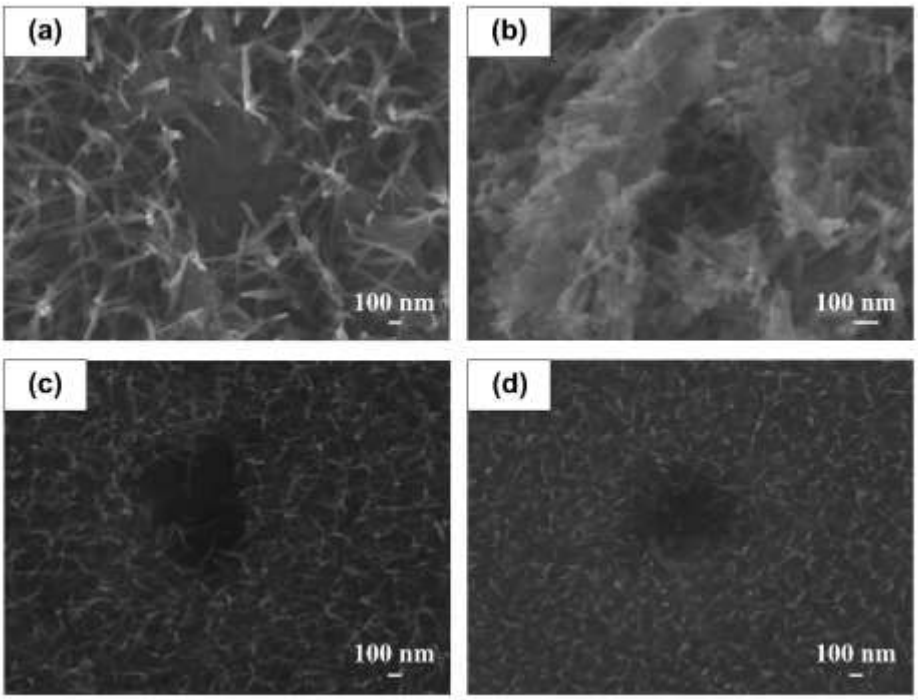

Figure 5: Indentation craters left by the Berkovich tip, at a peak load of 200 μN for (a) Base, (b) IncConc, (c) RedTemp and (d) RedTime samples.

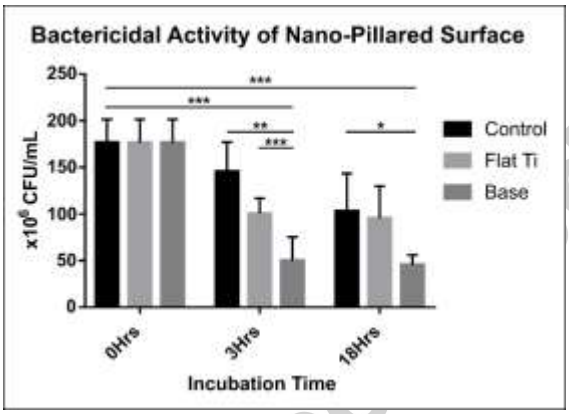

*Figure 6: Bactericidal efficiency of the nano-pillared surface. Comparison by 2-way ANOVA, *P<0.1, **P<0.01, ***P<0.001.*

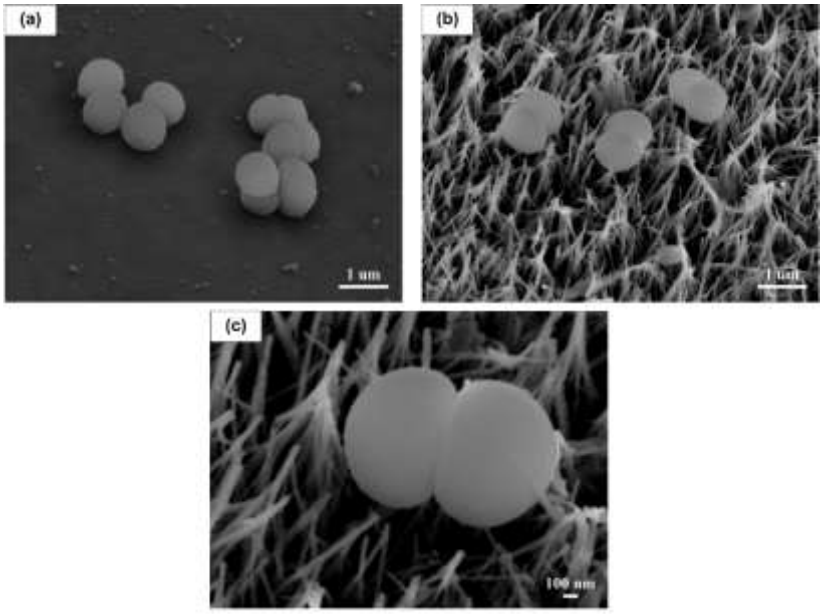

Figure 7: SEM images of S. aureus on (a) flat Ti-6Al-4V surface and (b, c) nano-textured surface (Base sample). Puncturing of bacterial cell shown in (c).

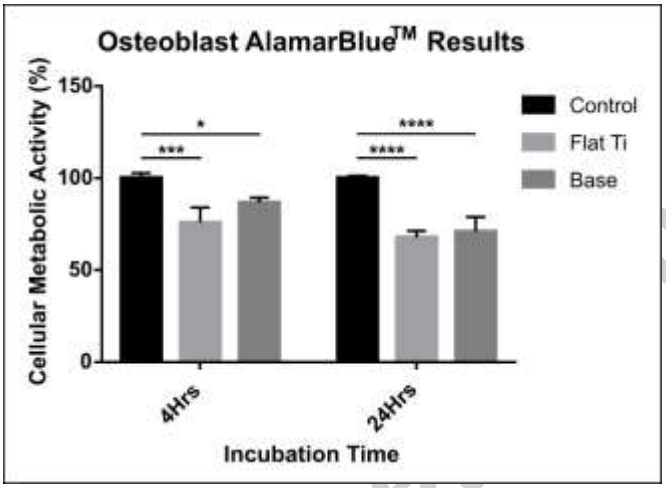

*Figure 8: Osteoblast AlamarBlueTM assay results. Comparison by 2-way ANOVA, *P<0.1, ***P<0.001, ****P<0.0001.*

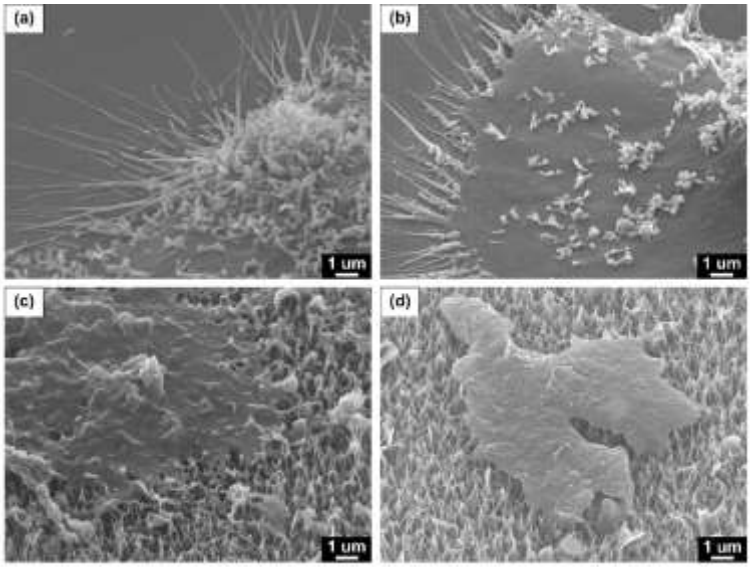

Figure 9: Osteoblast Cells fixed to flat Ti-6Al-4V surface (a, b) and nano-textured TiO2 Base surface (c, d). Images (a, c) taken after 4 hours incubation and (b, d) 24 hours incubation.

Table 1: Summary of hydrothermal experimental parameters

Sample Name	NaOH Concentration (M)	Reaction Temperature (°C)	Reaction Time (Hrs)
Base	1	240	3
IncConc	2	240	3
RedTemp	1	120	3
RedTime	1	240	1

Sample Name	Morphology	Average Structure Length (nm)	Average Structure Diameter (nm)
Base	Nanofibers	298 ± 33	52 ± 12
IncConc	Nanowire mesh	945 ± 254	43 ± 3
RedTemp	Nanostructures	348 ± 18	20 ± 2
RedTime	Nanostructures	251 ± 30	22 ± 3

Table 2: Surface morphology and average structure dimensions

Sample Name	Elastic Modulus (GPa)	Hardness (MPa)	Contact Depth (nm)
Base	12.2 ± 2.3	14.7 ± 1.8	606.9 ± 42.8
IncConc	20.1 ± 2.8	138.6 ± 76.6	193.0 ± 54.9

RedTemp	31.8 ± 0.9	221.3 ± 21.0	134.7 ± 6.7
RedTime	31.3 ± 1.5	222.6 ± 33.1	135.3 ± 13.3

Table 3: Nanoindentation results showing mechanical properties of the samples.

Highlights

- Hydrothermal synthesis parameters influence surface morphology, dictating surface mechanical properties
- Nano-textured surfaces have a 33% bactericidal efficiency against gram-positive *S. aureus* cells, after 18 hrs
- Human osteoblast cells have a 71% cellular metabolic activity when exposed to a nanowire array for 24 hrs